Systematic synthesis of $(Gd_{1-x}La_x)_2O_2SO_4:Tb^{3+}$ and $(Gd_{1-x}La_x)_2O_2S:Tb^{3+}$ nanophosphors for remarkably enhanced luminescence

Zhenqi Song[a], Fan Li[a], Sihan Feng[a], Zhiyuan Pan[a], Qi Zhu[a,*], Xudong Sun[a,b], Ji-Guang Li[c,*]

[a]*Key Laboratory for Anisotropy and Texture of Materials and School of Materials Science and Engineering, Shenyang, Liaoning, 110819, China*

[b]*Foshan Graduate School of Northeastern University, Foshan, Guangdong, 528311, China*

[c]*Research Center for Electronic and Optical Materials, National Institute for Materials Science, Tsukuba, Ibaraki, 305-0044, Japan*

Corresponding author

Dr. Qi Zhu

Northeastern University

Shenyang, China

E-mail: zhuq@smm.neu.edu.cn

Tel: +86-24-8367-2700

Dr. Ji-Guang Li

National Institute for Materials Science

Tsukuba, Japan

E-Mail: li.jiguang@nims.go.jp

Tel: +81-29-860-4394

Abstract

Coprecipitation with rare-earth nitrate, ammonium sulfate and ammonium hydroxide produced hydroxide-type amorphous precursors incorporating sulfate and carbonate anions, from which $[(Gd_{1-x}La_x)_{0.99}Tb_{0.01}]_2O_2SO_4$ and $[(Gd_{1-x}La_x)_{0.99}Tb_{0.01}]_2O_2S$ (x=0, 0.15, 0.3, 0.5, 0.65, 0.8, 1) were obtained as two series of nanophosphors by calcination at 950°C in air and hydrogen, respectively. The detailed characterization by XRD, SEM/TEM, BET and particle sizing confirmed that solid solutions were directly formed and that the products have small crystallite size, unimodal size distribution and high specific surface area, revealing the advantages of the synthesis method. Photoluminescence study revealed that La^{3+} admixture may significantly improve the 545 nm main emission of Tb^{3+} for both the phosphor series. Furthermore, the 545 nm main emission of $[(Gd_{1-x}La_x)_{0.99}Tb_{0.01}]_2O_2SO_4$ was identified to have an excellent thermal stability, which retained over 90% of its room temperature intensity at 150°C (no quenching for $Gd_2O_2SO_4:Tb^{3+}$). The two series of phosphors were comparatively studied for their excitation and luminescence performances, as a function of temperature and La^{3+} content, and the results were rationalized by considering bandgap, crystal structure, UV absorption, and the character of chemical bonds.

Keywords: $(Gd, La)_2O_2SO_4:Tb^{3+}$, $(Gd, La)_2O_2S:Tb^{3+}$, Solid solution, Nanophosphor, Photoluminescence

1. Introduction

Gd_2O_2S has an excellent X-ray blocking capacity by its high theoretical density (7.34 g/cm^2) and the large atomic number of Gd (Z = 64) and is chemically/structurally stable under high-energy radiation, so it is widely used for scintillation purposes.[1,2] The compound is also known to be an excellent host for photoluminescence, because of its wide band gap (~4.6-4.8 eV), low phonon energy (about 520 cm^{-1}), and good tolerance for activator doping.[3-5] Tb^{3+} doped Gd_2O_2S ($Gd_2O_2S:Tb^{3+}$) powder, for example, is widely used as a green phosphor in TV screens, cathode ray tubes and X-ray enhancement screens because of its high intrinsic conversion efficiency and high light yield.[6,7] Besides, $Gd_2O_2S:Tb^{3+}$ nano-colloid was reported to be a useful fluorescent probe in biomarkers.[8] The $Gd_2O_2S:Tb^{3+}$ bulk ceramic fabricated via sintering, on the other hand, finds important application in scintillation bio-probing, high-resolution neutron radiography and X-ray computed tomography (X-CT) for its excellent attenuation property, scintillation efficiency, and imaging quality.[9-11] Gd_2O_2S-based phosphors are conventionally synthesized via flux reaction at 1200-1300°C, which uses oxide and/or carbonate as the rare-earth (RE) source, elemental sulfur and/or sodium thiosulfate as the sulfur source and alkali carbonate and/or halide as a reflux.[12,13] Though the resulted powder has a high crystallinity because of its micron-sized large particles, contamination by alien cations and anions is hardly evitable. Treating a precursor with a sulfur-bearing gas[14,15] or combustion with thiourea as the fuel[16] may produce finer powders, but phase/chemical purity control is a frequent problem. Furthermore, the above methods all involved sulfur-containing toxic reactant and/or

exhaust gas.

The luminescence performance and application of $Gd_2O_2S:Tb^{3+}$ can be affected by a number of factors, such as particle morphology/granule size, chemical/phase purity, Tb^{3+} content, and lattice defects. For example, micron-sized particles are favored for phosphor application because of their better luminescence but are not satisfactory for the fabrication of scintillation ceramics because of their low specific surface area and poor sintering activity. It is also known that, by varying the concentration of Tb^{3+}, the emission color of $Gd_2O_2S:Tb^{3+}$ can be adjusted by the cross-relaxation process of Tb^{3+} ions.[17] Often, codoping of other ions can significantly affect the performance of $Gd_2O_2S:Tb^{3+}$. For example, Dy^{3+} can remarkably promote Tb^{3+} luminescence because there is a strong energy transfer from Dy^{3+} to Tb^{3+}.[18] Replacing some of the host Gd^{3+} ions with aliovalent Ta^{5+} or Sn^{4+} may create anion traps and eliminate the cation traps caused by sulfur vacancies and, therefore, enhances the main emission of $Gd_2O_2S:Tb^{3+}$.[19] Ca^{2+} and Ru^{4+} ions also have a strong influence on the defects in Gd_2O_2S, especially those caused by sulfur loss, even at a small concentration.[19] It is noteworthy that sulfur vacancy (Vs) instead of oxygen vacancy (Vo) is the dominant lattice defect in Gd_2O_2S, particularly in the scintillation ceramics fabricated by high-temperature sintering, since the formation energy of Vs is smaller than that of Vo.[20] This is in conformance with the soft-hard acid-base theory (HSAB),[21] which predicts that soft Lewis base S^{2-} is less affinitive than O^{2-} toward hard Lewis acid Gd^{3+}. As sulfur vacancies have a huge influence and may even completely quench luminescence,[22] suppressing the formation of such defects is essential to a high luminescence

performance of Gd_2O_2S-based phosphors/scintillation ceramics.

It should be noted that the stability of RE-S bond is significantly dependent on the ionic size of RE^{3+} (RE = La-Lu lanthanide, Y). Previous synthesis of RE_2O_2S by calcining the hydrothermally crystallized $RE_2(OH)_4SO_4{\cdot}nH_2O$ precursor compound in hydrogen ($RE_2(OH)_4SO_4{\cdot}nH_2O + 4H_2 \rightarrow RE_2O_2S + (n + 6)H_2O$) found that the strength of RE-S tends to decrease with decreasing ionic radius of RE^{3+} and Gd^{3+} happened to be the boundary for a pure product.[23,24] A similar observation was reported by other researchers in RE_2O_2S synthesis via thermolysis of RE chelate compounds in organic solvent.[25] In this regard, doping Gd_2O_2S with La^{3+} may strengthen the Gd-S bond, allowing for the fabrication of high-quality phosphors and bulk ceramics through suppressing the formation of sulfur vacancies. Furthermore, $La_2O_2S:Tb^{3+}$ itself (theoretical density ~5.83 g/cm^3) is an important green phosphor for X-ray excited luminescence (XEL) and cathodoluminescence (CL), and was revealed to be even more efficient than $Gd_2O_2S:Tb^{3+}$ for medium X-ray tube voltages.[6,26] Application of $La_2O_2S:Tb^{3+}$ for temperature sensing under UV excitation was also reported.[27] Though the mechanical mixtures of commercial $La_2O_2S:Tb^{3+}$ and $Gd_2O_2S:Tb^{3+}$ phosphor powders were previously investigated for luminescence,[6] a study can hardly be found in the literature for either (Gd, La)$_2O_2SO_4:Tb^{3+}$ or (Gd, La)$_2O_2S:Tb^{3+}$ solid solutions.

Although the aforesaid $RE_2(OH)_4SO_4{\cdot}nH_2O$ compound can serve as an excellent precursor to derive $RE_2O_2SO_4$ via annealing in air ($RE_2(OH)_4SO_4{\cdot}nH_2O \rightarrow RE_2O_2SO_4 + (n + 2)H_2O$; RE = La-Lu lanthanide and Y) and to derive RE_2O_2S (RE = La-Gd lanthanide) via annealing in hydrogen,[23,24,28] it cannot produce rounded nanoparticles because the compound easily crystallizes as submicron/micron sized flakes by its layered crystal structure, and the derived products tend to inherit a flaky particle morphology.[23,28] With the simple reactants of $RE(NO_3)_3$, $(NH_4)_2SO_4$ and NH_4OH, this

work produced hydroxide-like amorphous precursors containing both SO_4^{2-} and CO_3^{2-} anions via coprecipitation at ~4°C and pH=9 in open air, from which $[(Gd_{1-x}La_x)_{0.99}Tb_{0.01}]_2O_2SO_4$ and $[(Gd_{1-x}La_x)_{0.99}Tb_{0.01}]_2O_2S$ (x = 0, 0.15, 0.3, 0.5, 0.65, 0.8, 1.0) nanophosphors having a spherical particle morphology, good dispersion and narrow size distribution were successfully obtained via calcination at 950°C in air and hydrogen, respectively. The synthesis process avoided the use and emission of any sulfur-bearing hazardous substance and is more efficient than either the hydrothermal [23,28] or the thermolysis[25] method. More importantly, the incorporation of La^{3+} was confirmed to be able to significantly enhance Tb^{3+} luminescence for both the types of phosphors, and the $[(Gd_{1-x}La_x)_{0.99}Tb_{0.01}]_2O_2SO_4$ series were identified to possess an excellent thermal stability since they retained ~92-100% of their room temperature emission intensities at 150°C. In the following sections, we report the synthesis, characterization, and luminescence properties of the materials.

2. Experimental procedure

2.1 Raw materials and synthesis

The starting rare-earth materials for the experiments were Gd_2O_3, La_2O_3 and Tb_4O_7 (99.99% pure, Huizhou Ruier Rare Earth High-Tech Co., Ltd., Huizhou, China), which were separately dissolved with 1 mol/L nitric acid (analytical grade, Sinopharm Chemical Reagent Co., Ltd., Shanghai, China) to make nitrate solutions. Ultrapure water (resistivity >18 MΩ·cm) was used throughout the experiments. For powder synthesis, proper portions of the nitrate solutions were mixed together according to the formula of $[(Gd_{1-x}La_x)_{0.99}Tb_{0.01}]^{3+}$ (x=0, 0.15, 0.3, 0.5, 0.65, 0.8 and 1.0), followed by the addition of 15 mmol $(NH_4)_2SO_4$ (analytical grade, Sinopharm Chemical Reagent; $SO_4^{2-}/[(Gd_{1-x}La_x)_{0.99}Tb_{0.01}]^{3+}$ = 1.5 molar ratio) and volume adjustment of the reaction system to 100 ml. The mixed solution was cooled to ~4°C in an ice-water bath under

magnetic stirring, followed by dropwise addition of ammonium hydroxide solution (Sinopharm Chemical Reagent) until pH=9 to obtain precipitate.[29] After homogenization under magnetic stirring at ~4°C for 1 h, the precipitate was collected via centrifugation at 4000 rpm for 3 min, washed three times with water and once with anhydrous ethanol, and then dried in an oven at 60°C for 24 h. Finally, the fluffy precipitate (precursor) cake was lightly crushed with a mortar and pestle into a fine powder for characterization and further processing. $[(Gd_{1-x}La_x)_{0.99}Tb_{0.01}]_2O_2SO_4$ was produced by calcining the precursor powder in air at 950°C for 1 h and $[(Gd_{1-x}La_x)_{0.99}Tb_{0.01}]_2O_2S$ was obtained by calcining $[Gd_{1-x}La_x)_{0.99}Tb_{0.01}]_2O_2SO_4$ in hydrogen at the same temperature for 2 h, where a heating rate of 5°C /min was used for the rising phase of calcination.

2.2. Characterization techniques

Phase identification of the product was performed with an X-ray diffractometer (XRD; Model SmartLab, Rigaku, Tokyo, Japan) in the 2θ range of 10-70°, using nickel-filtered Cu Kα line (λ= 0.15406 nm) as the radiation source, an acceleration voltage/current of 40 kV/40 mA and a scan rate of 10° 2θ/min. Fourier transform infrared spectroscopy (FTIR; Model Nicolet iS5, Thermo Fisher Scientific, Madison, USA) was conducted by the standard KBr pellet method. The morphology and fine structure of the particles were analyzed using field emission scanning electron microscopy (FESEM, Model JSM-7001F, JEOL, Tokyo) at an acceleration voltage of 15 kV and transmission electron microscopy (TEM; Model FEI Talos F200X G2, Thermo Fisher Scientific) at 200 kV. Photoluminescence studies were performed in the temperature range of 25-250°C with an FP-8600 fluorescence spectrophotometer (JASCO, Tokyo), which was equipped with a Model ISF 513 (JASCO) integrating sphere (60 mm in diameter), a 150 W xenon lamp for excitation and a Model HPC-836 accessory (JASCO) for temperature control, and all the measurements were conducted

at a scan speed of 100 nm/min and a slit width of 5 nm. The spectral response of the spectrophotometer was corrected with a Rhodamine-B solution (5.5 g/L in ethylene glycol) and a standard light source unit (ECS-333, JASCO) for the ranges of 220–600 nm and 350–850 nm, respectively, and the quantum yield of luminescence was read out by a built-in analysis software of the equipment. The light absorption spectra of the samples were recorded using a UV-Vis-NIR spectrophotometer (Model UV-3600 Plus, Shimadzu, Kyoto, Japan). The specific surface area of the calcination product was measured by the Brunauer-Emmett-Teller (BET) method via nitrogen adsorption at 77 K, using a Model TriStar II 3020 instrument (Micromeritics, GA, USA). Particle sizing was conducted with a laser diffraction particle sizer (Model Zetasizer Nano ZS90, Malvern, UK), and the suspension for analysis was prepared by ultrasonic dispersion of 2.5 mg powder in 20 mL ethanol in the absence of surfactant.

3. Result and discussion

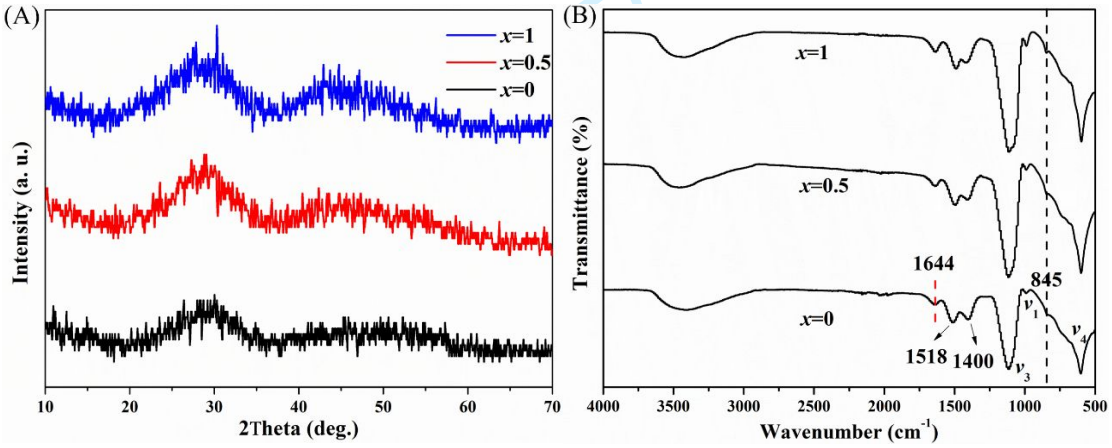

FIGURE 1 XRD patterns (A) and FTIR spectra (B) for the typical precursors of x = 0, 0.5 and 1.0.

Figure 1A shows the XRD patterns of three typical precursors (x = 0, 0.5, 1.0) obtained by the coprecipitation method, from which it is seen that they all exhibited an amorphous character. To assess chemical composition, the precursors were subjected to FTIR analysis, and the results are exhibited in Figure 1B. It was found that the three samples have virtually the same spectral features, and all showed a broad and strong

absorption in the ~3000-3750 cm^{-1} region for the vibration of hydroxyl groups (~3500-3750 cm^{-1}) and the stretching of O-H bond in water molecules (~3000-3500 cm^{-1}). The shallow peak at ~1644 cm^{-1} further proved the presence of molecular water and can be assigned to the H-O-H bending mode of H_2O. SO_4^{2-} absorptions are clearly identifiable at ~1100, 980, and 610 cm^{-1}, which correspond to v_3, v_1, and v_4 vibrations, respectively.[30] The other three absorption peaks at ~1518, 1398 and 845 cm^{-1} were caused by CO_3^{2-} [29,30] owing to solution absorption of ambient CO_2. The results thus indicated that the precursors would be $Ln_2(OH)_{4-2m}(CO_3)_m(SO_4)\cdot nH_2O$ (Ln = $(Gd_{1-x}La_x)_{0.99}Tb_{0.01}$), where the $SO_4^{2-}/[(Gd_{1-x}La_x)_{0.99}Tb_{0.01}]^{3+}$ molar ratio was assigned to be 1/2 because all the precursors directly transformed into $[(Gd_{1-x}La_x)_{0.99}Tb_{0.01}]_2O_2SO_4$ by annealing in air at 950°C. The precursor of this work can be viewed as a derivative of the aforesaid $RE_2(OH)_4SO_4\cdot nH_2O$ sulfate hydroxide since its composition can be resulted by replacing a part of the hydroxyls in $RE_2(OH)_4SO_4\cdot nH_2O$ with CO_3^{2-} anions. FE-SEM observation (Figure S1) showed that all the three samples, unlike the hydrothermally produced $RE_2(OH)_4SO_4\cdot nH_2O$, are loose agglomerates of nanosized spherical particles, which is beneficial to derivation of dispersed nanophosphors by calcination. Previous analysis via thermogravimetry in flowing air (heating rate 10°C /min) showed that $RE_2(OH)_4SO_4\cdot nH_2O$ would yield $RE_2O_2SO_4$ in the temperature ranges of ~405-1300°C for RE = La, ~440-1120°C for RE = Gd and ~450-1110°C for RE = Tb,[23] and $RE(OH)CO_3$ would decompose into RE_2O_3 via removal of hydroxyls and then carbonate anions up to ~800°C.[31] We thus selected 950°C as a suitable annealing temperature to derive $[(Gd_{1-x}La_x)_{0.99}Tb_{0.01}]_2O_2SO_4$ from the $Ln_2(OH)_{4-2m}(CO_3)_m(SO_4)\cdot nH_2O$ precursors.

Figure 2A shows the XRD patterns of the products after calcination in air at 950°C, and it was found that they can all be indexed with the standard diffractions of monoclinic $Gd_2O_2SO_4$ (JCPDS No.24-9775). The XRD spectra steadily drifted toward

lower diffraction angles with increasing x (La^{3+} content), which is due to more replacement of Gd^{3+} by larger La^{3+} (1.10 Å for La^{3+} and 1.00 Å for Gd^{3+} under 7-fold coordination). We analyzed the XRD patterns with the Jade 6 software, and found that lattice constants a, b and c and cell volume V all almost linearly increase with increasing x value. This clearly indicated that (Gd, La)$_2O_2SO_4$:Tb^{3+} solid solutions have been formed. Broadening analysis of the XRD peaks with Scherrer formula revealed that the x = 0, 0.15, 0.3, 0.5, 0.65, 0.8 and 1.0 products have average crystallite sizes of ~31.3, 30.8, 28.7, 27.4, 20.7, 22.6, and 76.5 nm, respectively. It is seen that, despite the same calcination condition, the average crystallite size of $La_2O_2SO_4$:Tb^{3+} (x = 1.0) is much larger than that of $Gd_2O_2SO_4$:Tb^{3+} (x = 0). This is due to the fact that the hydroxyls and carbonate anions in the precursor of $La_2O_2SO_4$:Tb^{3+} can be removed at lower temperatures,[23] which allowed more growth of the $La_2O_2SO_4$:Tb^{3+} crystallites. Meanwhile, the crystallite sizes of the other samples are smaller than those of the x = 0 and 1.0 ones. This could be due to higher degrees of lattice distortion by La^{3+} substitution, which caused more broadening of the XRD peaks.

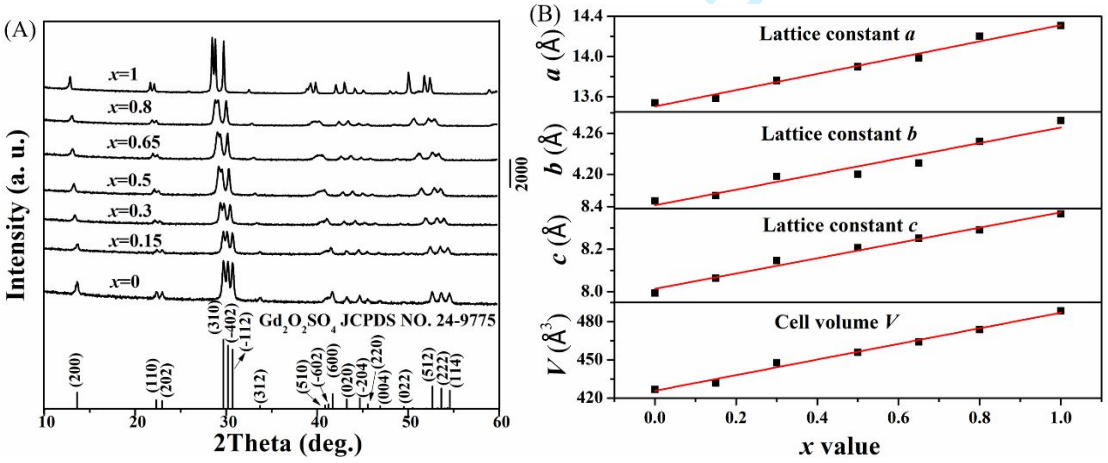

FIGURE 2 XRD patterns (A) and lattice parameters and cell volume (B) of the powders obtained by calcining the precursors at 950°C in air.

FE-SEM observation of the three typical [$(Gd_{1-x}La_x)_{0.99}Tb_{0.01}$]$_2O_2SO_4$ powders (x =

0, 0.5, 1.0) indicated that they similarly contain porous agglomerates of primary particles/crystallites (Figure 3A-C) but the $La_2O_2SO_4:Tb^{3+}$ sample appeared coarser. BET analysis found that the $x = 0$, 0.5 and 1.0 powders have specific surface areas (S_{BET}) of ~11.43, 10.7 and 7.12 m^2/g. The sphere-equivalent particle size Ds (nm) of a powder can be derived via equation $Ds = 6000/(S_{BET} \times D)$, where D is the theoretical density (g/m^3) of the material. The $x = 0$, 0.5 and 1.0 compositions were calculated to have D values of 6.80, 6.15 and 5.50 g/m^3 with the monoclinic unit cell and their cell volumes (Figure 2B) and, therefore, have Ds values of 77, 90 and 153 nm, respectively. The Ds of $La_2O_2SO_4:Tb^{3+}$ ($x = 1.0$) is much larger than those of the other two, and this conforms to the results of FE-SEM observation (Figure 3A-C). We also analyzed the particle size distribution of these three powders via laser diffraction, and the results are exhibited in Figure 3D-F. It is seen that they favorably have a unimodal size distribution in each case and have peak sizes of ~250, 215 and 257 nm for $x = 0$, 0.5 and 1.0, respectively.

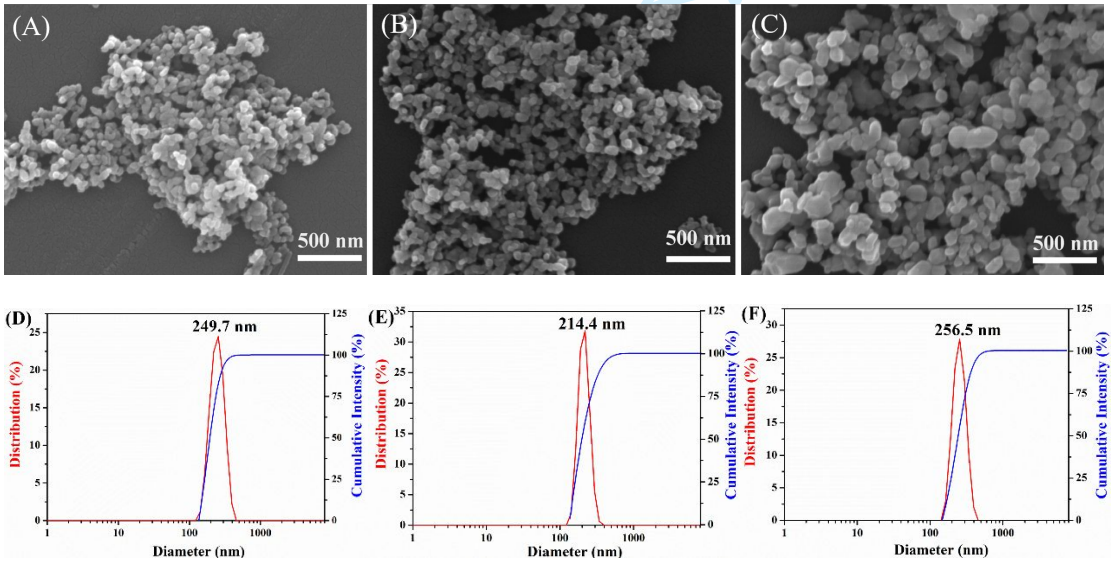

FIGURE 3 FE-SEM morphologies (A-C) and particle size distributions (D-F) for the three typical $[(Gd_{1-x}La_x)_{0.99}Tb_{0.01}]_2O_2SO_4$ powders of $x = 0$ (A, D), $x = 0.5$ (B, E) and $x = 1.0$ (C, F).

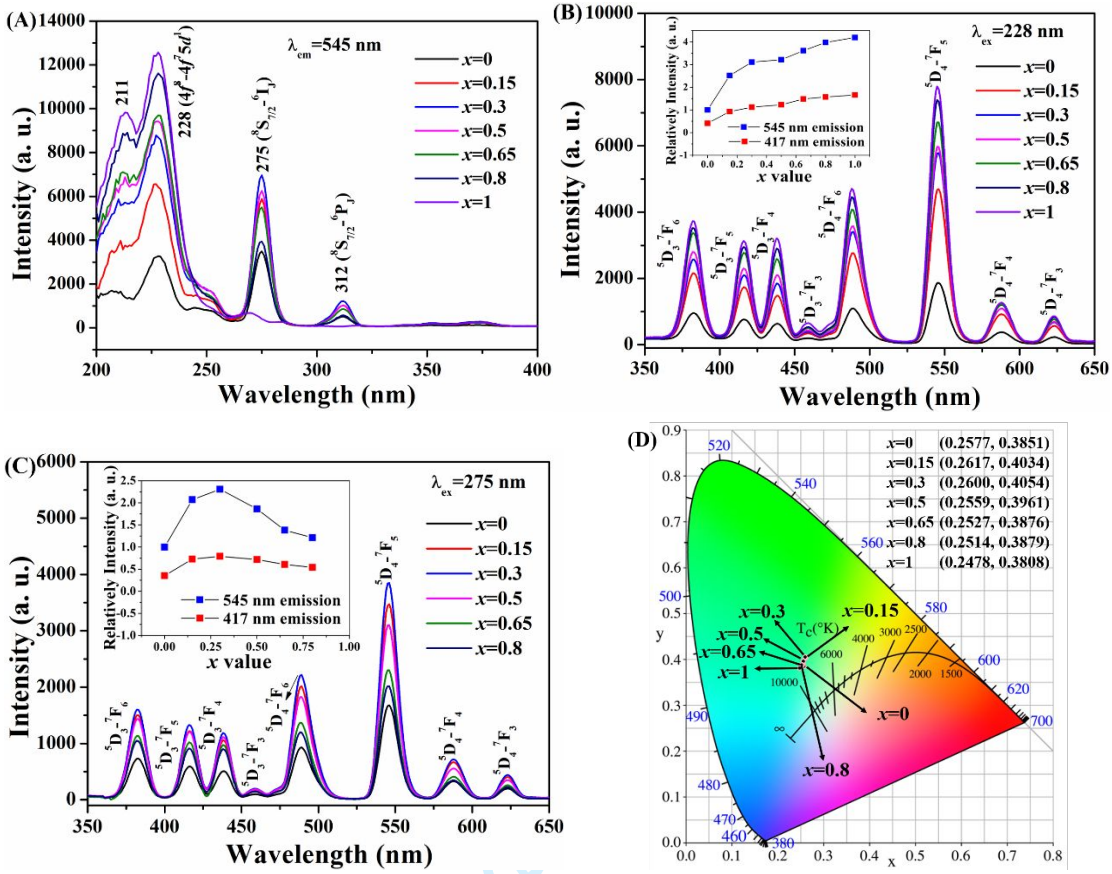

FIGURE 4 The photoluminescence spectra of $(Gd_{1-x}La_x)_2O_2SO_4:Tb^{3+}$, where (A) is for excitation (PLE, λ_{em} = 545 nm) and (B) and (C) are for emission (PL) under 228 and 275 nm excitation, respectively. Part (D) presents the CIE color coordinates for the luminescence under 228 nm excitation. The insets in parts (B) and (C) are relative intensities of the 417 and 545 nm emissions, where the 545 nm emission intensity of the x = 0 sample was normalized to 1.

Figure 4A shows the excitation spectra (PLE) of the series of $[(Gd_{1-x}La_x)_{0.99}Tb_{0.01}]_2O_2SO_4$ phosphor powders, which were obtained by detecting the 545 nm green emission of Tb^{3+}. The double split peaks centered at ~211 and 228 nm were assigned to the low-spin and high-spin $4f^8$-$4f^7 5d^1$ transitions of Tb^{3+}, respectively. Host excitation was not considered herein since the materials did not show light absorption above 200 nm (bandgap >6.2 eV, Figure S2). The bandgap energy of either $La_2O_2SO_4$ or $Gd_2O_2SO_4$ has not been reported before to best of our knowledge. The $^8S_{7/2}$-^6I_J and $^8S_{7/2}$-^6P_J intra-$4f^7$ transitions of Gd^{3+} were also observed at ~275 and 311 nm[32] for the Gd^{3+}-containing samples, respectively. The presence of Gd^{3+} excitation implies the

occurrence of $Gd^{3+} \rightarrow Tb^{3+}$ energy transfer.[33] It is clear that the $4f^8$-$4f^75d^1$ excitation of Tb^{3+} monotonically gained intensity with increasing La^{3+} content. This could be due to gradually stronger ionicity of the host lattice, since the electronegativity of La ($\chi = 1.1$) is smaller than that of Gd ($\chi = 1.2$), which improved the efficiency of excitation through decoupling Tb^{3+} electrons with host lattice. Figure 4B shows the emission spectra (PL) obtained under 228 nm excitation of the powders, where the $^5D_{3,4}$-^7F_J (J = 3-6) luminescence of Tb^{3+} can be readily identified. The intensity of PL successively increased with increasing La^{3+} content, following the trend observed from the $4f^8$-$4f^75d^1$ excitation intensity, and the 545 nm main emissions of the x = 0.15 and 1.0 compositions are ~2.5 and 4.2 times as strong as that of $Gd_2O_2SO_4$:Tb^{3+} ($x = 0$, the inset of Figure 4B). The luminescence of Tb^{3+} is mediated by the host Gd^{3+} ions in this work (except for the case of x =1.0), which involves relaxation of the 228 nm excitation energy to the $^6I_J/^6P_J$ levels of Gd^{3+} followed by energy transfer to the $^5D_{3,4}$ states of Tb^{3+}. In this regard, the enhanced PL by La^{3+} doping is mainly owing to reduced consumption of the 228 nm excitation energy by Gd^{3+}, which includes energy migration among the Gd^{3+} ions themselves, non-radiative relaxation, and $^6P_J \rightarrow {}^8S_{7/2}$ emission (~312 nm). Noteworthy is that the luminescence from $^5D_3$ energy level is quite strong (bule/green intensity ratio I_{417}/I_{545} = 0.41, I_{438}/I_{545} = 0.34). This implies that $Tb^{3+}(^5D_3)$ + $Tb^{3+}(^7F_6)$ = $Tb^{3+}(^5D_4)$ + $Tb^{3+}(^7F_0)$ cross relaxation, which quenches $^5D_3$ emission, is not significant. The powders were assayed from their PL spectra to have CIE color coordinates of around (0.26, 0.40), corresponding to a cyan color (Figure 4D). We also analyzed the luminescence through exciting the host Gd^{3+} ions with 275 nm UV light

($^8S_{7/2}$-^6I_J transition), and the results are presented in Figure 4C. It is seen that the PL spectra are essentially identical to those of Figure 4B, but the intensities of both the $^5D_3$-^7F_J and $^5D_4$-^7F_J emissions first increase with increasing La^{3+} doping up to $x = 0.3$ and then steadily decrease. Such a phenomenon may be explained by considering that (1) replacing Gd^{3+} with a proper amount of La^{3+} (x up to ~0.3) reduces the number density of Gd^{3+} ions, which alleviates the aforesaid energy consumption by Gd^{3+} and, therefore, enhances $Gd^{3+} \rightarrow Tb^{3+}$ energy transfer, and (2) a high enough La^{3+} content (x > ~0.3) may elongate the separation distance of neighboring Gd^{3+} and Tb^{3+} ions to such an extent that the efficiency of $Gd^{3+} \rightarrow Tb^{3+}$ energy transfer decreases.

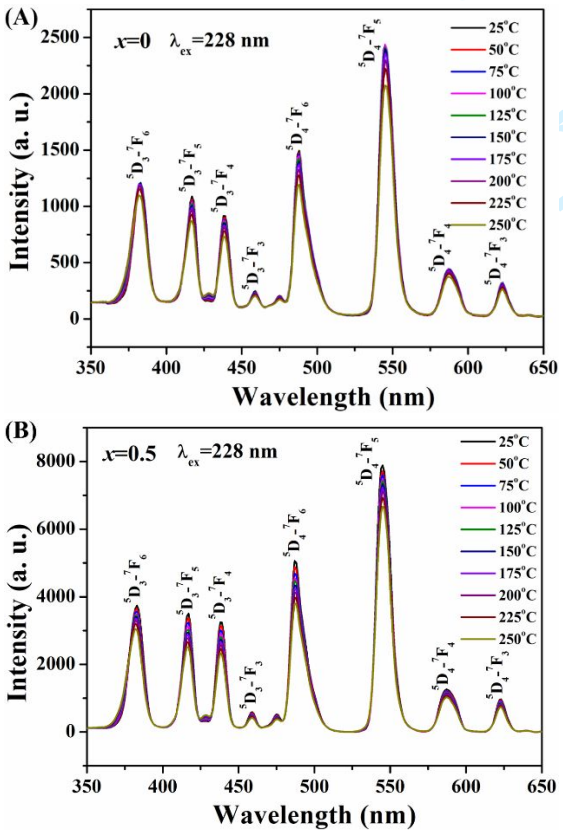

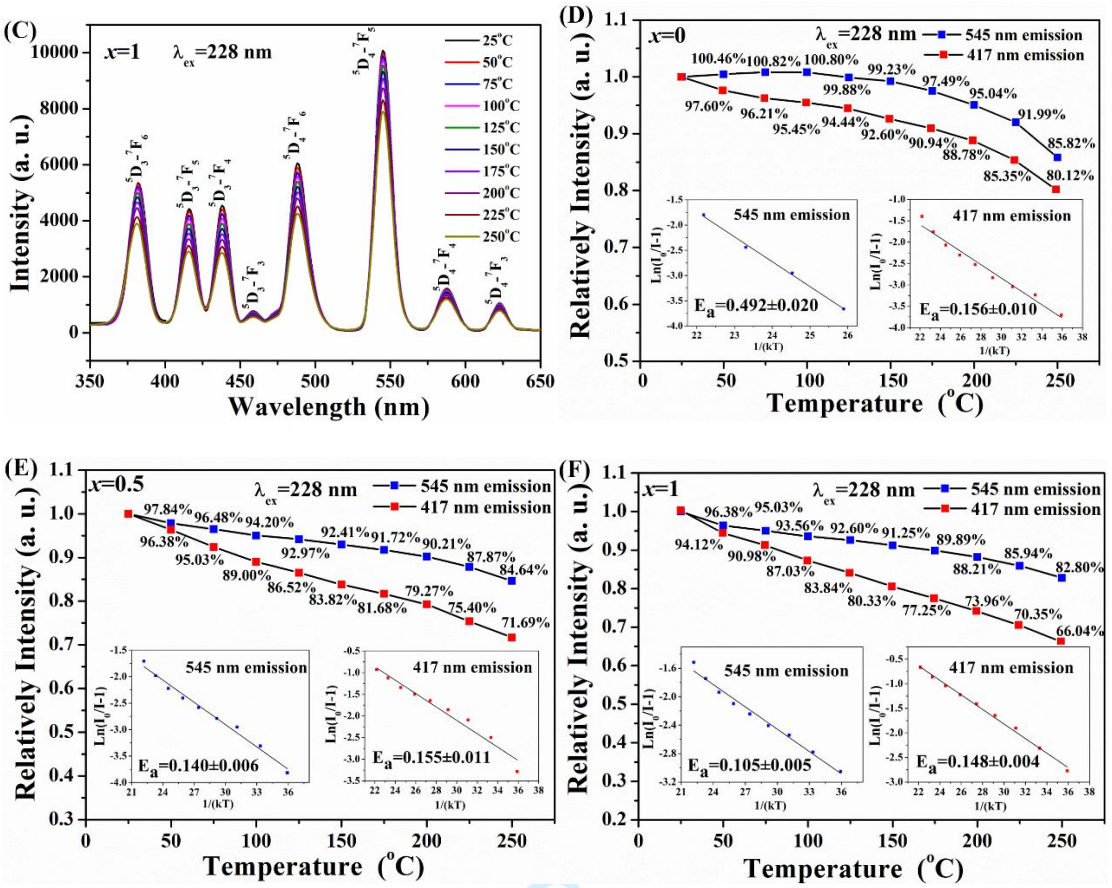

FIGURE 5 Temperature-dependent PL spectra (A-C) and relative intensities of the 417 and 545 nm emissions as a function of measurement temperature (D-F) for the x = 0 (A, D), x = 0.5 (B, E) and x = 1.0 (C, F) typical phosphors. The insets in (D-F) show the plots for determination of the activation energy of thermal quenching.

The thermal stability of luminescence was analyzed for the three typical phosphors of x = 0, 0.5 and 1.0, and the results are displayed in Figure 5. It was observed from the temperature-dependent PL spectra that raising the measurement temperature from 25 to 250°C did not induce any new emission and did not alter the position of each existing peak (Figure 5A-C). Of particular interest is that both the 545 nm green and 417 nm blue emissions showed high stability against temperature increase, and respectively retained over 90% and 80% of their room temperature intensities at 150°C (Figure 5D-F), a temperature frequently used to evaluate whether a phosphor is suitable for high power LED application. Especially, the $Gd_2O_2SO_4:Tb^{3+}$ phosphor (x = 0) almost has no

intensity loss up to 150°C for the 545 nm emission, and the 417 nm emission kept as high as ~92.6% of its room temperature intensity at 150°C. Such an excellent thermal stability implies that thermal ionization of Tb^{3+} (promotion of Tb^{3+} electrons into conduction band) hardly took place owing to the wide bandgap (above ~6.2 eV) and high structure stiffness (low phonon-energy) of $(Gd, La)_2O_2SO_4$. Monoclinic $RE_2O_2SO_4$ (space group: C_2/c) has a unique layered crystal structure, which is constructed by alternative stacking of $[RE_2O_2]^{2+}$ main layers and interlayer SO_4^{2-}.[23,24,28] In such a structure, each $[SO_4]$ tetrahedron provides three O atoms to form REO_7 one-capped trigonal prim that serves as the building block of the main layer. The strong pillaring effect of interlayer SO_4^{2-} may restrain thermal vibration of the RE containing main layers to render a high structure rigidity. It was observed that the 417 nm emission lost intensity slightly faster than the 545 nm one with increasing temperature in each case, which could be due to thermal relaxation of some of the $^5D_3$ electrons to the $^5D_4$ level of Tb^{3+}. Besides, the thermal stability of luminescence tends to decrease with increasing La^{3+} content, and this might be due to the lattice expansion (Figure 2B; lattice softening) caused by La^{3+} doping. The activation energy of thermal quenching (E_a) can be derived from the following equation[34]:

$$I(T) = I_0/[1 + c\exp(-E_a/(kT)] \quad (1)$$

where I_0 and $I(T)$ are the luminous intensities at room temperature and measurement temperature T (in Kelvin), respectively, k is the Boltzmann constant (8.617×10^{-5} eV), and c is a pre-exponential constant. The insets in Figure 5D-F show $\mathrm{Ln}(I_0/I–1)$ versus $1/(kT)$ transformation of the experimental data, and linear fitting yielded E_a values of

~0.492, 0.140 and 0.105 eV for the 545 nm emission and ~0.156, 0.155 and 0.148 eV for the 417 nm emission of the x = 0, 0.5 and 1.0 samples, respectively. It should be noted that the E_a of the 545 nm emission of $Gd_2O_2SO_4:Tb^{3+}$ (x = 0) was determined with the temperature range where thermal quenching of luminescence took place (175-250°C).

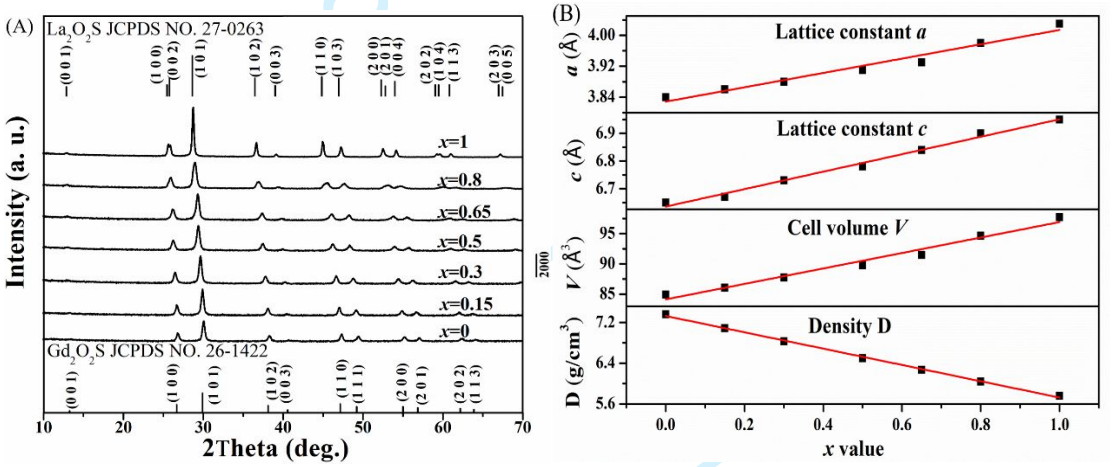

FIGURE 6 The XRD patterns (A) and lattice parameters and theoretical densities (B) of the powders calcined at 950°C in H_2.

Figure 6A shows the XRD patterns of the products after calcination at 950°C in hydrogen, where it can be found that the diffraction peaks can be indexed with those of the hexagonal structured Gd_2O_2S (P-3m1 space group; JCPDS No. 26-1422) in each case and the peaks gradually shifted toward lower diffraction angles with increasing La^{3+} doping (x value). Analysis of the XRD patterns with the Jade 6 software confirmed the formation of solid solution, since lattice constants a and c (a = b) and cell volume V almost linearly expanded with increasing x. Broadening analysis of the XRD peaks

with Scherrer formula found that the x = 0, 0.15, 0.3, 0.5, 0.65, 0.8 and 1.0 powders have average crystallite sizes of ~30, 24.9, 24.2, 21.5, 17.7, 15.5 and 42.2 nm, respectively. Such a tendency of size variation follows that of the (Gd, La)$_2$O$_2$SO$_4$:Tb^{3+} series, but in each case the average crystallite size of (Gd, La)$_2$O$_2$S:Tb^{3+} is smaller than that of (Gd, La)$_2$O$_2$SO$_4$:Tb^{3+}. This is due to disintegration of the (Gd, La)$_2$O$_2$SO$_4$:Tb^{3+} crystallites by the occurrence of (Gd, La)$_2$O$_2$SO$_4$:Tb^{3+} + 4H$_2$ → (Gd, La)$_2$O$_2$S:Tb^{3+} + 4H$_2$O reduction reaction and reconstructive phase transition.

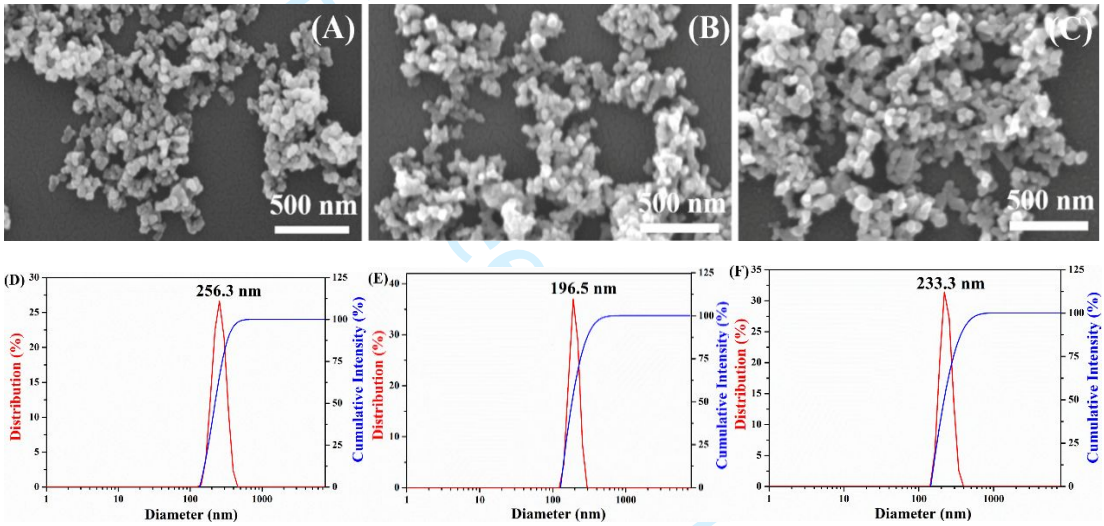

FIGURE 7 FE-SEM morphologies (A-C) and particle size distributions (D-F) for the (Gd$_{1-x}$La$_x$)$_2$O$_2$S:Tb^{3+} powders of x = 0 (A, D), x =0.5 (B, E) and x=1.0 (C, F).

FE-SEM analysis showed that the three typical (Gd$_{1-x}$La$_x$)$_2$O$_2$S:Tb^{3+} powders, like their (Gd$_{1-x}$La$_x$)$_2$O$_2$SO$_4$:Tb^{3+} counterparts (Figure 3A-C), are porous agglomerates of the primary particles/crystallites (Figure 7A-C). Laser diffraction particle sizing confirmed that the three powders also have unimodal size distributions, which are centered at ~256, 197 and 233 nm for x = 0 (Figure 7D), x = 0.5 (Figure 7E) and x = 1.0 (Figure 7F), respectively. Such a size distribution would be beneficial to the construction of a uniform phosphor screen for scintillation and cathodoluminescence

and to the sintering of high-quality ceramic scintillators. BET analysis found that the x = 0, 0.5 and 1.0 powders have specific surface areas of ~17.3, 16.7 and 15.7 m^2/g, which correspond to sphere-equivalent average particle sizes of ~47, 55 and 66 nm, respectively, according to the theoretical densities shown in Figure 6B.

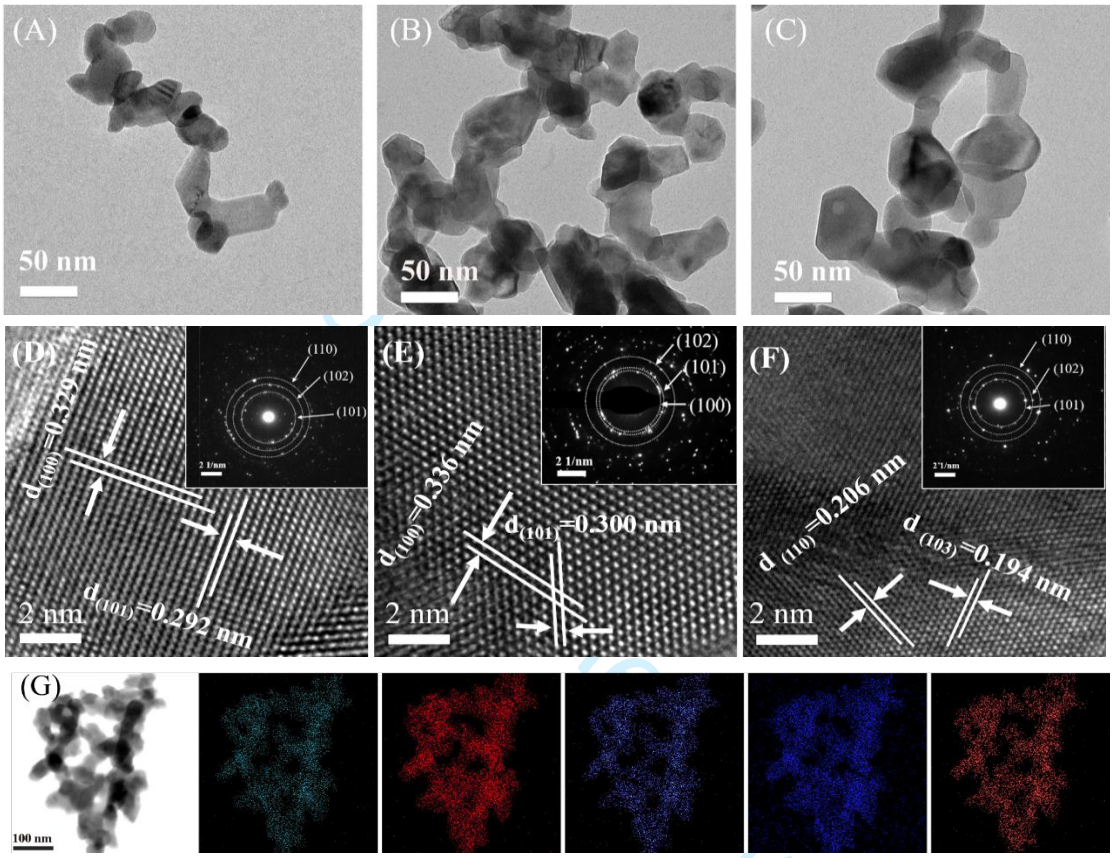

FIGURE 8 TEM morphologies (A-C) and lattice images (D-F) for the $(Gd_{1-x}La_x)_2O_2S:Tb^{3+}$ powders of x = 0 (A, D), x = 0.5 (B, E) and x = 1.0 (C, F). Part (G) shows the results of elemental mapping for the x = 0.5 sample, and the insets in parts (D-F) are the corresponding SAED patterns.

TEM analysis was performed for the three typical $(Gd_{1-x}La_x)_2O_2S:Tb^{3+}$ samples to understand finer microstructure, and the results are shown Figure 8A-F. Low magnification observation showed that a number of the primarily crystallites were glued together to form small clusters (Figure 8A-C), which explains why the particle size revealed by laser diffraction is much larger than the average crystallite size assayed via Scherrer equation. The individual crystallites (~20-50 nm) tend to be faceted, implying

a high degree of crystallization, as also revealed by the clear lattice fringes (Figure 8D-F) and the spot-like selected area electron diffractions (SAED, the insets in Figure 8D-F). Analyzing the lattice fringes found that the (100) and (101) crystal planes of $Gd_2O_2S:Tb^{3+}$ ($x = 0$) have *d*-spacings of ~0.329 and 0.292 nm, respectively, which are smaller than the ~0.336 nm for (100) and ~0.300 nm for (101) of $(Gd_{0.5}La_{0.5})_2O_2S:Tb^{3+}$ ($x = 0.5$). This indicates lattice expansion by La^{3+} doping. Elemental mapping with the $(Gd_{0.5}La_{0.5})_2O_2S:Tb^{3+}$ midway composition showed that the constituent elements of Gd, La, Tb, O and S are all uniformly distributed across the crystallites (Figure 8G). The results thus provided firm evidence for the formation of solid solution. Besides, the (101), (102), (110) and (103) planes of the $La_2O_2S:Tb^{3+}$ ($x = 1$) end composition can be clearly identified via lattice imaging and SAED analysis, and the measured *d*-spacings of ~0.310, 0.2480, 0.200 and 0.194 nm are close to the 0.3128, 0.2470, 0.2024 and 0.1938 nm reported in the standard diffraction file of La_2O_2S (JCPDS No. 27-0623), respectively.

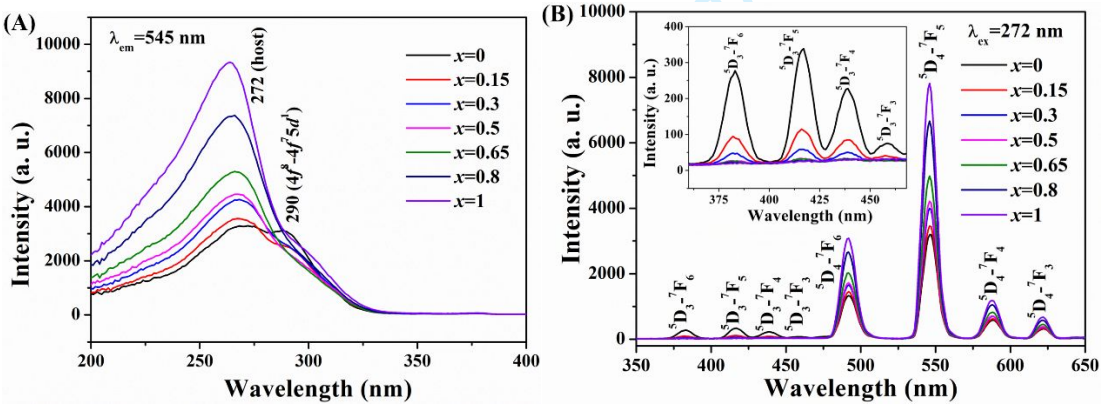

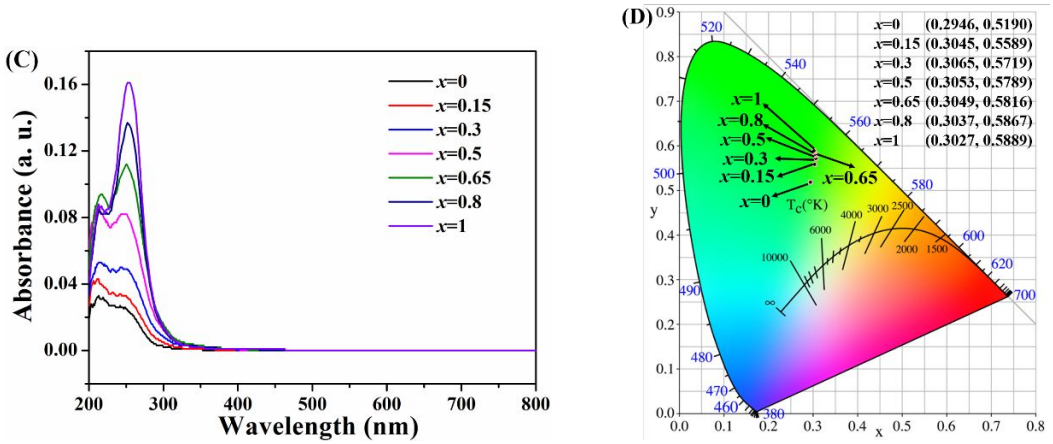

FIGURE 9 PLE (A), PL (B) and UV-vis absorption (C) spectra and the CIE color coordinates of luminescence (D) for the series of $(Gd_{1-x}La_x)_2O_2S:Tb^{3+}$ phosphors.

Figure 9A shows the PLE spectra of the series of $(Gd_{1-x}La_x)_2O_2S:Tb^{3+}$ phosphors (λ_{em} = 545 nm), where a broad band up to ~325 nm is clearly seen in each case. The band is overlapped from host excitation (centered at ~272 nm; promotion of electrons from the valence band to the conduction band of $(Gd_{1-x}La_x)_2O_2S$) and $4f^8 \rightarrow 4f^7 5d^1$ inter-configurational transition of Tb^{3+} (at ~290 nm).[35] The appearance of $4f^8 \rightarrow 4f^7 5d^1$ excitation as a sub-band implies that the centroid of the 5*d* energy level of Tb^{3+} is close to the bottom of the conduction band of $(Gd_{1-x}La_x)_2O_2S$. The $^8S_{7/2}$-^6I_J and $^8S_{7/2}$-^6P_J transitions of Gd^{3+}, which occurred at ~275 and 311 nm in $(Gd_{1-x}La_x)_2O_2SO_4:Tb^{3+}$, respectively, were buried in the wide and strong excitation band and are not identifiable. Noteworthy is that the intensity of host excitation steadily gained intensity and the $4f^8 \rightarrow 4f^7 5d^1$ excitation of Tb^{3+} gradually lost intensity against host excitation with increasing La^{3+} content. Figure 9B shows the PL spectra of $(Gd_{1-x}La_x)_2O_2S:Tb^{3+}$, which were taken under host excitation at 272 nm. It is clear that, as observed from the $(Gd_{1-x}La_x)_2O_2SO_4:Tb^{3+}$ series in Figure 4B, each of the $^5D_4$-^7F_J (J = 3-6) emissions of Tb^{3+} monotonically gained intensity at a higher La^{3+} content, following the tendency observed from that of host excitation, and the 545 nm main emission ($^5D_4$-$^7F_5$ transition)

of $La_2O_2S:Tb^{3+}$ (x = 1.0) is ~2.5 times as strong as that of $Gd_2O_2S:Tb^{3+}$ (x = 0). The $^5D_3$-^7F_J luminescence of Tb^{3+}, on the contrary, gradually lost intensity with increasing La^{3+} substitution, and was completely quenched when x reached ~0.5 (the inset in Figure 9B). The series of phosphors were analyzed to have quantum yields (QYs) of ~31.6, 30.9, 32.8, 32.6, 39.3, 47.0 and 58.6% for x = 0, 0.15, 0.3, 0.5, 0.65, 0.8 and 1.0, respectively. Noteworthy is that the QYs of the $(Gd_{1-x}La_x)_2O_2SO_4:Tb^{3+}$ series cannot be credibly determined, since the most effective excitation wavelength of 228 nm is very close to the shorter end of the corrected spectral region (220-850 nm). It is also seen from Figure 9D that the $(Gd_{1-x}La_x)_2O_2S:Tb^{3+}$ phosphors emit a green color in each case, but the CIE color coordinates slightly drifted toward the green corner with increasing x, especially for the x = 0-0.5 samples, owing to the gradually weaker $^5D_3$-^7F_J emissions. To understand the effect of La^{3+} on excitation and emission, UV-vis spectroscopy was conducted on the series of $(Gd_{1-x}La_x)_2O_2S:Tb^{3+}$ phosphors and the results are shown in Figure 9C. It is seen that the capability of UV absorption (up to ~325 nm, peaking at ~254 nm) is steadily stronger with increasing La^{3+} content. This indicates that La_2O_2S has a larger absorption coefficient than Gd_2O_2S, though data are not available from the literature, and enhanced UV absorption is the main reason for the gradually higher intensities of host excitation and $^5D_4$-^7F_J luminescence. Though credible determination of bandgap energy (E_g) is difficult with the absorption spectra, owing to the mixing in of Tb^{3+} transition (Figure 9A), theoretical analysis indicated that Gd_2O_2S has an Eg of ~4.2-4.6 eV[36,37] and La_2O_2S has a smaller value of ~2.91 Ev.[38] It can then be inferred that the Eg of $(Gd, La)_2O_2S$ will decrease with increasing La^{3+} content, owing to

downward shifting of the bottom of the conduction band (CB). This will in turn causes the 5*d* energy level and $^5D_3$ state of Tb^{3+} to move closer to the edge of CB. As a result, $^5D_3$ electrons may move into CB more easily under thermal fluctuation, and this explains the gradually weaker and eventually quenched $^5D_3$-^7F_J luminescence with increasing La^{3+} content (Figure 9B). The lack of $^5D_3$ emissions in $La_2O_2S:Tb^{3+}$ crystal was indeed reported to be due to the burying of $^5D_3$ level in CB.[39]

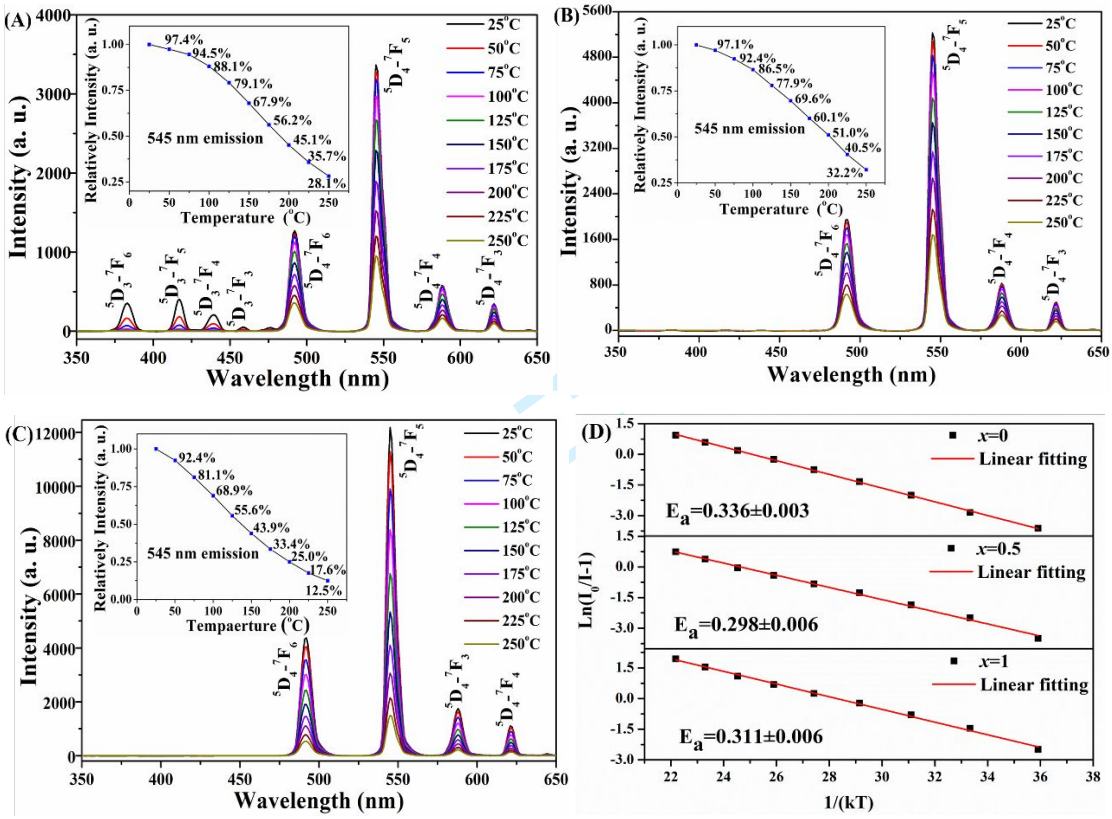

FIGURE 10 Temperature-dependent PL spectra (A-C; λ_{ex} = 272 nm) and determination of the activation energy of thermal quenching for the 545 nm emission of the x = 0, 0.5 and 1.0 phosphors (D). The insets in parts (A)-(C) show relative intensity of the 545 nm emission as a function of measurement temperature.

Figure 10A-C exhibits the temperature-dependent PL spectra for the three $(Gd_{1-x}La_x)_2O_2S:Tb^{3+}$ phosphors of x = 0, 0.5 and 1.0. Though new emission did not appear in the measured temperature range of 25-250°C, the $^5D_4$-^7F_J luminescence was steadily weakened with increasing temperature, and the 545 nm emission retained ~68% (x =

0), 70% (x = 0.5) and 44% (x = 1.0) of its room temperature intensity at 150°C. While $^5D_3$-^7F_J luminescence is hardly observable for the x = 0.5 and 1.0 samples, that of the x = 0 sample gradually lost intensity at a higher temperature and was almost completely quenched at ~125°C owing to thermal promotion of $^5D_3$ electrons to the conduction band as aforesaid. Comparing Figure 10A-C with Figure 5D-F showed that the $(Gd_{1-x}La_x)_2O_2S:Tb^{3+}$ phosphors have a significantly faster rate of luminescence quenching than $(Gd_{1-x}La_x)_2O_2SO_4:Tb^{3+}$ in each case. This is primarily owing to the smaller bandgap and more covalent chemical bonds of $(Gd_{1-x}La_x)_2O_2S$. Though 7-fold coordinated in both the types of compounds, $(Gd, La)^{3+}$ is bonded with seven O atoms in $(Gd_{1-x}La_x)_2O_2SO_4$ but with four O and three S atoms in $(Gd_{1-x}La_x)_2O_2S$.[24,28] The much smaller electronegativity of S (χ = 2.58 for S and χ = 3.44 for O) makes $(Gd_{1-x}La_x)_2O_2S$ remarkably more covalent (less ionic) than $(Gd_{1-x}La_x)_2O_2SO_4$, which enhances electron-host coupling and lowers the thermal stability of luminescence through raising the possibility/intensity of photon-phonon interaction. It is also seen from the insets of Figure 10A-C that $La_2O_2S:Tb^{3+}$ (x = 1.0) has the lowest thermal stability among the three $(Gd_{1-x}La_x)_2O_2S:Tb^{3+}$ phosphors. Aside from the considerations from cell volume (lattice stiffness), bandgap and bond covalency, thermal promotion of $^5D_4$ electrons into the conduction band could also be a possible reason for the severe quenching of $La_2O_2S:Tb^{3+}$, since the $^5D_4$ excited state of Tb^{3+} lies only ~0.4 eV below the bottom of CB, as roughly estimated with the theoretical bandgap energy of La_2O_2S (2.91 eV)[38] and the emission wavelength of $^5D_4 \rightarrow {}^7F_6$ transition (492 nm, 2.52 eV). With the experimental data shown in Figure 9A-C, the activation energies (E_a) of thermal

quenching were assayed by linear fitting of the Ln[$I_0/I(T)$-1] versus 1/(kT) plots to be ~0.336, 0.298 and 0.311 eV for the x = 0, 0.5 and 1.0 phosphors, respectively. Though E_a values of ~0.31 eV[40] and 0.25 eV[41] were reported for $Gd_2O_2S:Tb^{3+}$ (x = 0), our literature survey failed to find E_a data for the x = 0 and 0.5 phosphors.

4. Conclusion

The series of precursors obtained by coprecipitation have the general chemical formula of $[(Gd_{1-x}La_x)_{0.99}Tb_{0.01}]_2(OH)_{4-2m}(CO_3)_m(SO_4)\cdot nH_2O$ (x = 0-1.0), which yielded $[(Gd_{1-x}La_x)_{0.99}Tb_{0.01}]_2O_2SO_4$ by calcination in air at 950°C for 1 h. Calcining $[(Gd_{1-x}La_x)_{0.99}Tb_{0.01}]_2O_2SO_4$ in hydrogen at 950°C for 2 h then produced $[(Gd_{1-x}La_x)_{0.99}Tb_{0.01}]_2O_2S$. Both the series of powders are nanocrystalline solid solutions having high specific surface area and unimodal particle-size distribution. The $[(Gd_{1-x}La_x)_{0.99}Tb_{0.01}]_2O_2SO_4$ nanophosphors showed strong $^5D_{3,4}$-^7F_J (J = 3-6) luminescence under 228 nm excitation ($4f^8 \rightarrow 4f^7 5d^1$ transition of Tb^{3+}), which steadily gained intensity at a high La^{3+} content. The 545 nm main emission of these phosphors has a high thermal stability and kept over 90% of its room-temperature intensity at 150°C. The series of $[(Gd_{1-x}La_x)_{0.99}Tb_{0.01}]_2O_2S$ nanophosphors showed strong $^5D_4$-^7F_J but much weaker $^5D_3$-^7F_J luminescence under 272 nm excitation (host excitation). The intensity of $^5D_4$-^7F_J luminescence successively increased while that of $^5D_3$-^7F_J decreased with increasing La^{3+} content, and the emission from $^5D_3$ was completely quenched when x reached ~0.5. $[(Gd_{1-x}La_x)_{0.99}Tb_{0.01}]_2O_2S$ has a much lower thermal stability than its $[(Gd_{1-x}La_x)_{0.99}Tb_{0.01}]_2O_2SO_4$ counterpart, and that of $La_2O_2S:Tb^{3+}$ is the lowest among the typical compositions of x = 0, 0.5 and 1.0. The observed results of luminescence

were explained by considering bandgap, crystal structure, excitation absorption, and the character of chemical bonds.

Declaration of Competing Interest

The authors declare that they have no known competing financial interests or personal relationships that could have appeared to influence the work reported in this paper.

Acknowledgment

This work is supported in part by the National Natural Science Foundation of China (Grant No. 52172112, 51972047).

References

1. Liu Q, Pan HM, Chen X, Li XY, Liu X, Li W, et al. Gd_2O_2S:Tb scintillation ceramics fabricated from high sinterability nanopowders via hydrogen reduction. Opt Mater. 2019;94:299-304.
2. Wang XJ, Meng QH, Li MQ, Wang XJ, Wang ZH, Zhu Q, et al. A low temperature approach for photo/cathodoluminescent Gd_2O_2S:Tb (GOS:Tb) nanophosphors. J Am Ceram Soc. 2018;102:3296-306.
3. Qian BF, Wang YL, Zhao QR, Duan TZ, Zhou XQ, Zou HF, et al. Adjustable multi-color luminescence and energy transfer of capsule-shaped Gd_2O_2S: Tb^{3+}, Sm^{3+} phosphors. J Lumin. 2022;244:11875.
4. Ning L, Lu LP, Sun HY, Zhang XY, Bai ZH, Mi XY. Study on improving the performance of Gd_2O_2S:Er^{3+},Yb^{3+} up-conversion phosphors by Lu^{3+} introduction. J Alloy Compd. 2022;922:166632.
5. Lin SL, Liu TY, Lo CL, Wang BS, Lee YJ, Lin KY, et al. Synthesis, surface modification, and photophysical studies of Ln_2O_2S:Ln^{3+}(Ln=Gd, Tb, Eu; Ln=Tb and/or Eu) nanoparticles for luminescence bioimaging. J Lumin. 2016;175:165-75.
6. Kandarakis I, Cavouras D. Experimental and theoretical assessment of the performance of Gd_2O_2S:Tb and La_2O_2S:Tb phosphors and Gd_2O_2S:Tb-La_2O_2S:Tb mixtures for X-ray imaging. Eur Radiol. 2001;11:1083-91.
7. Zhou Y, Li F, Wang XJ, Zhu Q, Li XD, Sun XD, et al. Facile synthesis of $Gd_2O_2SO_4$:Tb and Gd_2O_2S:Tb green phosphor nanopowders of unimodal size distribution and photoluminescence. Adv Powder Technol. 2021;32:1911-9.
8. Hernández-Adame L, Méndez-Blas A, Ruiz-García J, Vega-Acosta JR, Medellín-Rodríguez FJ, Palestino G. Synthesis, characterization, and photoluminescence properties of Gd:Tb oxysulfide colloidal particles. Chem Eng J. 2014;258:136-45.
9. Machado IP, Teixeira VC, Pedroso CCS, Brito HF, Rodrigues LCV. X-ray scintillator Gd_2O_2S:Tb^{3+} materials obtained by a rapid and cost-effective microwave-assisted solid-state

synthesis. J Alloy Compd. 2019;777:638-45.
10. Tang B, Yin W, Wang QB, Chen L, Huo HY, Wu Y, et al. High Quantum Efficiency Rare-Earth-Doped Gd_2O_2S:Tb,F Scintillators for Cold Neutron Imaging. Molecules. 2023;28:1815.
11. Kandarakis I, Cavouras D, Prassopoulos P, Kanellopoulos E, Nomicos CD, Panayiotakis GS. Evaluating scintillators used in radiation detectors of medical imaging systems by the effective fidelity index method. Eur J Radiol. 1999;30:61-6.
12. Chatterjee S, Shanker V, Chander H. Thermoluminescence of Tb doped Gd_2O_2S phosphor. Mater Chem Phys. 2003;80:719-24.
13. Ding YJ, Yang WM, Zhang QT, Wang LX. Influence of alkali metal compound fluxes on Gd_2O_2S:Tb particle and luminescence. J Mate Sci. 2015;26:1982-6.
14. Tian Y, Cao W-H, Luo X-X, Fu Y. Preparation and luminescence property of Gd_2O_2S:Tb X-ray nano-phosphors using the complex precipitation method. J Alloy Compd. 2007;433:313-7.
15. Xing MM, Cao WH, Pang T, Ling XQ, Chen N. Preparation and characterization of monodisperse spherical particles of X-ray nano-phosphors based on Gd_2O_2S:Tb. Chin Sci Bull. 2009;54:2982-6.
16. Fu ZL, Geng Y, Chen HW, Zhou SH, Yang HK, Jeong JH. Combustion synthesis and luminescent properties of the Eu^{3+}-doped yttrium oxysulfide nanocrystalline. Opt Mater. 2008;31:58-62.
17. Silva A, Cebim MA, Davolos MR. Excitation mechanisms and effects of dopant concentration in Gd_2O_2S:Tb^{3+} phosphor. J Lumin. 2008;128:1165-8.
18. Zhang WH, Kou HM, Ge L, Zhang Y, Lin L, Li W. Effects of doping ions on the luminescence performance of terbium doped gadolinium polysulfide phosphor. J Phys Conf Ser. 2020;1549:032064.
19. Morlotti R, Magro C, Vedda A, Martini M, Croci S, Nikl M. The Effect of Co-Doping by Ca^{2+}, Ta^{5+}, Sn^{4+}, and Ru^{4+} Ions on the X-Ray Luminescent Properties of Gd_2O_2S: Tb^{3+} Phosphors. J Electrochem Soc. 2003;150:H81-84.
20. Wang W, Kou HM, Liu SP, Shi Y, Li J, Feng XQ. Optical and scintillation properties of Gd_2O_2S:Pr,Ce,F ceramics fabricated by spark plasma sintering. Ceram Int. 2015;41:2576-81.
21. Pearson R G. Hard and Soft Acids and Bases. J Am Ceram Soc. 1963;85:3533-9.
22. Blahuta S, Viana B, Bessiere A, Mattmann E, LaCoure B. Luminescence quenching processes in Gd_2O_2S:Pr^{3+},Ce^{3+}scintillating ceramics. Opt Mater. 2011;33:1514-8.
23. Wang XJ, Li J-G, Molokeev MS, Wang XJ, Liu WG, Zhu Q, et al. Hydrothermal crystallization of a $Ln_2(OH)_4SO_4{\cdot}nH_2O$ layered compound for a wide range of Ln (Ln=La-Dy), thermolysis, and facile transformation into oxysulfate and oxysulfide phosphors. RSC Adv. 2017;7:13331-9.
24. Wang XJ, Molokeev MS, Zhu Q, Li J-G. Controlled hydrothermal crystallization of anhydrous $Ln_2(OH)_4SO_4$ (Ln=Eu-Lu, Y) as a new family of layered rare earth metal hydroxides. Chem Eur J. 2017;23:16034-43.
25. Gu J, Ding Y, Ke J, Zhang YW, Yan CH. Controllable synthesis of monodispersed middle and heavy rare earth oxysulfide nanoplates based on the principals of HSAB theory. Acta Chim Sin. 2013;71:360-6.
26. Sklensky AF, Buchanan RA, Maple TG, Bailey HN. Quantum Utilization in X-Ray Intensifying Screens. IEEE Trans Nucl Sci. 1974;21:685-91.
27. Yap SV, Ranson RM, Cranton WM, Koutsogeorgis D. Decay time characteristics of La_2O_2S:

Eu and La_2O_2S:Tb for use within an optical sensor for human skin temperature measurement. Appl Optics. 2008;47:4895.

28. Wang XJ, Li J-G, Molokeev MS, Zhu Q, Li XD, Sun XD. Layered hydroxyl sulfate: Controlled crystallization, structure analysis, and green derivation of multi-color luminescent $(La,RE)_2O_2SO_4$ and $(La,RE)_2O_2S$ phosphors (RE = Pr, Sm, Eu, Tb, and Dy). Chem Eng J. 2016;302:577-86.
29. Luo ZQ, Li F, Zhu Q, Sun XD, Li J-G. Low-temperature green synthesis of nanocrystalline $La_2O_2S:Pr^{3+}$ powders and investigation of photoluminescence. J Mater Res Technol. 2022;17:2540-2549.
30. Gadssen JA. Infrared spectra of minerals and related inorganic compounds. Newton, MA: Butterworths; 1975.
31. Li J-G, Li XD, Sun XD, Ikegami T, Ishigaki T, et al. Uniform Colloidal Spheres for $(Y_{1-x}Gd_x)_2O_3$ (x=0-1): Formation Mechanism, Compositional Impacts, and Physicochemical Properties of the Oxides. Chem Mat. 2008;20:2274-81.
32. Song LX, Du PF, Jiang QX, Cao HB, Xiong J. Synthesis and luminescence of high brightness $Gd_2O_2SO_4:Tb^{3+}$ nanopieces and the enhanced luminescence by alkali metal ions co-doping, J Lumin. 2014;150:50-54.
33. Zhang Y, Lv JW, Ding N, Jiang S, Zheng T, Li JY. Tunable luminescence and energy transfer from Gd^{3+} to Tb^{3+} ions in silicate oxyfluoride scintillating glasses via varying Tb^{3+} concentration, J Non-Cryst Solids. 2015;423:30-34.
34. Dorenbos P. Thermal quenching of Eu^{2+} 5d-4f luminescence in inorganic compounds. J Phys Condens Matter. 2005;17:8103-11.
35. Gorokhova EI, Demidenko VA, Mikhrin SB, Rodnyi PA, van Eijk CWE. Luminescence and scintillation properties of Gd_2O_2S:Tb,Ce ceramics. IEEE Trans Nucl Sci. 2006;52:3129-32.
36. Raukas M, Mishra KC, Peters C, Schmidt PC, Johnson KH, Choi J, et al. Electronic structure and associated properties of $Gd_2O_2S;Tb^{3+}$. J Lumin. 2000;87:980-2
37. Ding YJ, Wang LX, Zhang QT, Pan SB. Enhanced Luminescence of La^{3+}-Doped Gadolinium Oxysulfide with Tunable Crystalline Size. J Electron Mater. 2017;46:5986-5994.
38. Shah K, Ćirić A, Murthy KVR, Chakrabarty BS. Investigation of a new way of synthesis for nano crystallites of La_2O_2S & 1%Ln (Ln = Pr, Eu, Tb, Dy, Er) doped La_2O_2S and study their structural and optical properties. J Alloys Compd. 2021;851:156725.
39. Ratinen H. X-ray-excited optical fluorescence of ten rare earth ions in Y_2O_2S, La_2O_2S, and Gd_2O_2S. Phys Status Solidi A. 2010;12:447-51.
40. Wang XJ, Wang XJ, Wang ZH, Zhu Q, Zhu G, Wang C, et al. Photo/cathodoluminescence and stability of Gd_2O_2S:Tb,Pr green phosphor hexagons calcined from layered hydroxide sulfate. J Am Ceram Soc. 2018;101:5477-86.
41. Xia ZG, Liu RS, Huang KW, Drozd V. $Ca_2Al_3O_6F:Eu^{2+}$:a Green-Emitting Oxyfluoride Phosphor for White Light-Emitting Diodes. J Mater Chem. 2012;22:15183-9.

Supporting Information

Systematic synthesis of $(Gd_{1-x}La_x)_2O_2SO_4:Tb^{3+}$ and $(Gd_{1-x}La_x)_2O_2S:Tb^{3+}$ nanophosphors for remarkably enhanced luminescence

Zhenqi Song[a], Fan Li[a], Sihan Feng[a], Zhiyuan Pan[a], Qi Zhu[a,*], Xudong Sun[a,b], Ji-Guang Li[c,*]

[a]*Key Laboratory for Anisotropy and Texture of Materials and School of Materials Science and Engineering, Shenyang, Liaoning, 110819, China*

[b]*Foshan Graduate School of Northeastern University, Foshan, Guangdong, 528311, China*

[c]*Research Center for Electronic and Optical Materials, National Institute for Materials Science, Tsukuba, Ibaraki, 305-0044, Japan*

Corresponding author
Dr. Qi Zhu
Northeastern University
Shenyang, China
E-mail: zhuq@smm.neu.edu.cn
Tel: +86-24-8367-2700

Dr. Ji-Guang Li
National Institute for Materials Science
Tsukuba, Japan
E-Mail: li.jiguang@nims.go.jp
Tel: +81-29-860-4394

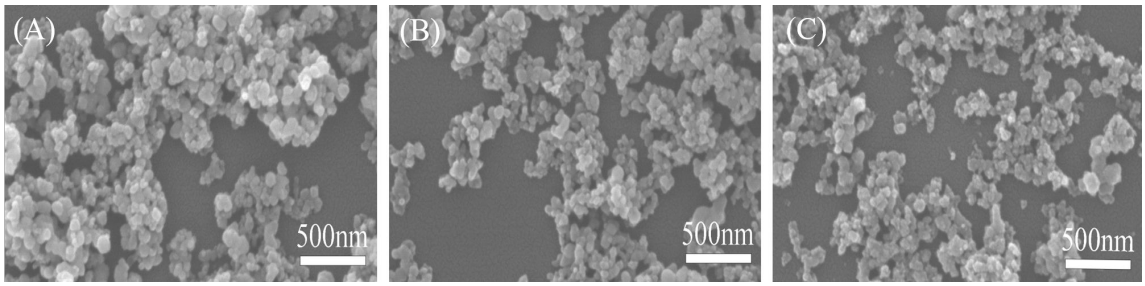

Fig. S1. FE-SEM morphologies of the three typical precursors of x = 0 (A), 0.5 (B) and 1.0 (C).

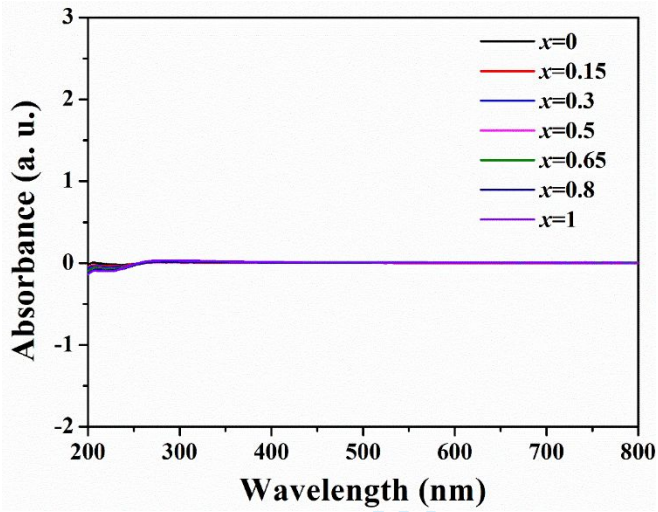

Fig. S2. UV-vis absorption spectra of the series of (Gd, La)$_2$O$_2$SO$_4$:Tb^{3+} powders.